Landslides (2013) 10:815–829
DOI 10.1007/s10346-013-0417-1
Received: 11 July 2012
Accepted: 16 May 2013
Published online: 30 June 2013

E. Brückl · F. K. Brunner · E. Lang · S. Mertl · M. Müller · U. Stary

The Gradenbach Observatory—monitoring deep-seated gravitational slope deformation by geodetic, hydrological, and seismological methods

Abstract The Gradenbach mass movement (GMM) is an example of DGSD (deep-seated gravitational slope deformation) in crystalline rocks of the Eastern Alps (12.85°E, 47.00°N). The main body of the GMM covers an area of 1.7km^2 and its volume is about 120×10^{6}m^3. A reconstruction of the deformation history yields a mean displacement of ~22m from 1962 to 2011. In 1965/66, 1975, 2001, and 2009 high sliding velocities, exceeding several meters per year, interrupt the quasi-stationary periods of slow movement (≤0.3m/year). Since 1999 the displacement of the main body of the GMM has been observed by GPS. Time series of extensometer readings, precipitation, snow cover water equivalent, water discharge, and hydrostatic water level observed in boreholes were re-processed and are presented in this paper. Continuous recording of seismic activity by a seismic monitoring network at the GMM began in the summer of 2006. Deformation has been monitored since 2007 by an embedded strain rosette based on fiber optics technology and a local conventional geodetic deformation network. The velocity of the GMM could be modeled to a large extent by a quantitative relation to hydro-meteorological data. During the phase of high sliding velocity in spring 2009, the seismic activity in the area increased significantly. Several types of seismic events were identified with some of them preceding the acceleration of the main body by about 6 weeks. The potential inherent in the Gradenbach Observatory data to supply early warning and hazard estimation is discussed.

Keywords Deep-seated gravitational slope deformation (DSGD) · GPS · Hydrology · Seismic monitoring · Early warning

Introduction

The Gradenbach mass movement (GMM) is located in the Gradenbach valley near its junction with the Möll valley northwest of the village Döllach, Austria (12.85°E, 47.00°N). It is an example of deep-seated gravitational slope deformation (DGSD, e.g., Dramis and Sorriso-Valvo 1994)) in crystalline rocks of the Eastern Alps. It covers an area of ~1.7 km^2 and its volume was estimated to be 120×10^6 m^3 using refraction seismic measurements and borehole data (Brückl and Brückl 2006). Several historical documents support the assumption that the development of the GMM from an inactive or very slow deforming DGSD to its current active state is a young geological process. The rural settlement of the area of the GMM took place during the eighteenth century according to historical records of the township of Döllach and we may assume that no indications of dangerous slope deformations were observed at that time. Häusler (1974) describes photographs from 1870 and 1880–1885, where slope movements can already be recognized in the gorge of the Gradenbach. Kronfellner-Kraus (1974) showed by comparing an 1826 cadastral map with a 1967 aerial photograph of the area that during these 141 years some landmarks have been shifted up to 60 m. Other reports of activity at the GMM date back to 1917 (Kronfellner-Kraus 1980). Probably the most prominent movements were catastrophic events in 1965 and 1966, triggered by high precipitation. The foot of the landslide moved beyond the surface of separation and damaged torrent barrages. High discharge of the Gradenbach caused massive erosion at the toe and catastrophic debris flows developed, which destroyed the village of Putschall near the junction of the Gradenbach and the Möll valley (Kronfellner-Kraus 1974).

After the 1965–1966 disasters, geodetic, geotechnical, and hydrological monitoring was initiated (Kronfellner-Kraus 1980; Lang and Stary 2011). The episodically occurring high velocities of the GMM and the existing monitoring data since the 1965–1966 disasters (e.g., Moser and Kiefer 1988; Weidner et al. 1998a, 1998b) provided motivation to concentrate monitoring activities at GMM within the frame of ISDR (International Strategy for Disaster Reduction) and IDNDR (International Decade of Natural Disaster Reduction). GPS measurements started in 1999 (Brunner et al. 2003). Continuous seismic monitoring data of the GMM from 2006 onwards is available (Mertl and Brückl 2007) and an integrated base of hydrological and meteorological monitoring data since 1999 has been established.

The Gradenbach Observatory consists of the currently operating geodetic, hydrological, hydro-meteorological, and seismological monitoring systems as well as the facilities for near real-time evaluation of the data sets and their systematic archiving. Main goals of the Gradenbach Observatory, addressed by this study, are to understand the relation between the sliding velocity and hydro-meteorological parameters, to provide an early warning system, and to provide a realistic estimate of the potential hazards of the GMM.

Geology, structure, and kinematics

The GMM is located in the central Eastern Alps at the southern edge of the Tauern window (Fig. 1). Over 25 km of penninic (ophiolitic) and sub-penninic units (Fig. 2) were exhumed in this tectonic window during the Miocene (e.g., Fügenschuh et al. 1997). These units form a dome-shaped structure, dipping to the south below the Upper East-Alpine Schober crystalline (see cross section in Fig. 2). The deepest unit is the sub-penninic Venediger nappe followed by the penninic Glockner nappe and the Matrei zone.

The GMM is part of the Matrei zone, which consists mainly of phyllitic Bündner-schists, carbonates, and Alpine Verrucano (Fig. 2). The phyllitic Bündner-schists are less resilient and more susceptible to mass movements than the para- and ortho-gneisses of the Schober crystalline in the southwest and the prasinites and amphibolites of the Glockner nappe in the northeast. However, the calcareous mica-schists of the Gockner nappe near the northeastern boundary of the main body also show high deformity and represent a mostly continuous transition to the GMM.

A digital terrain model with a 10-m grid interval (courtesy BEV—Bundesamt für Eich-und Vermessungswesen; Vienna, Austria) of the GMM is shown in Fig. 3a as shaded relief. The boundary of the GMM generally follows the description by Moser and Glumac (1983). Color coded contours of the thickness of the main body of the

Fig. 1 Regional geological setting of the GMM (Gradenbach Mass Movement): major geological units (Schmid et al. 2004) are superimposed on a digital elevation model (courtesy of *BEV* Bundesamt für Eich- und Vermessungswesen, Vienna, Austria); *rectangle* outlines the extent of a detailed geological map of the GMM as shown in Fig. 2

GMM are superimposed. Photos from viewpoints 1–4 (Fig. 3a) illustrate the morphology of the crown, the main scarp, the highly fractured rock cut by the road, and the deeply incised Gradenbach valley at the toe of the mass movement. The delineation of the high infiltration area at the surface (Fig. 3a) corresponds to Moser and Glumac's model of the mass movement. It does not necessarily correlate with the rock mechanical properties of the main body at greater depth. However, it is very important for the ratio between the surface runoff and the percolation of rain and snowmelt water.

The depth to the compact base of the GMM was determined by refraction seismic measurements (Brückl 1984; Brückl and Brückl 2006). From these data and the information from two boreholes

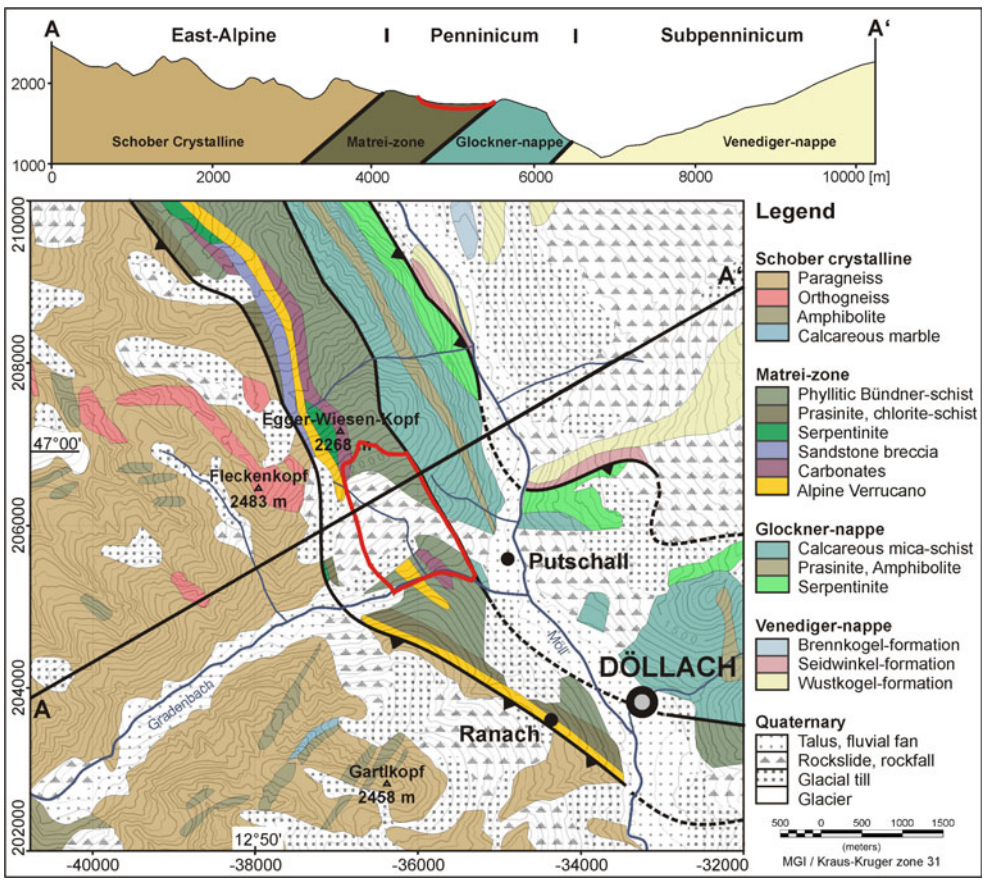

Fig. 2 Geology and tectonic setting of the GMM adapted from "Geologische Karte von Salzburg 1:200 000", Geologische Bundesanstalt, Wien, 2005

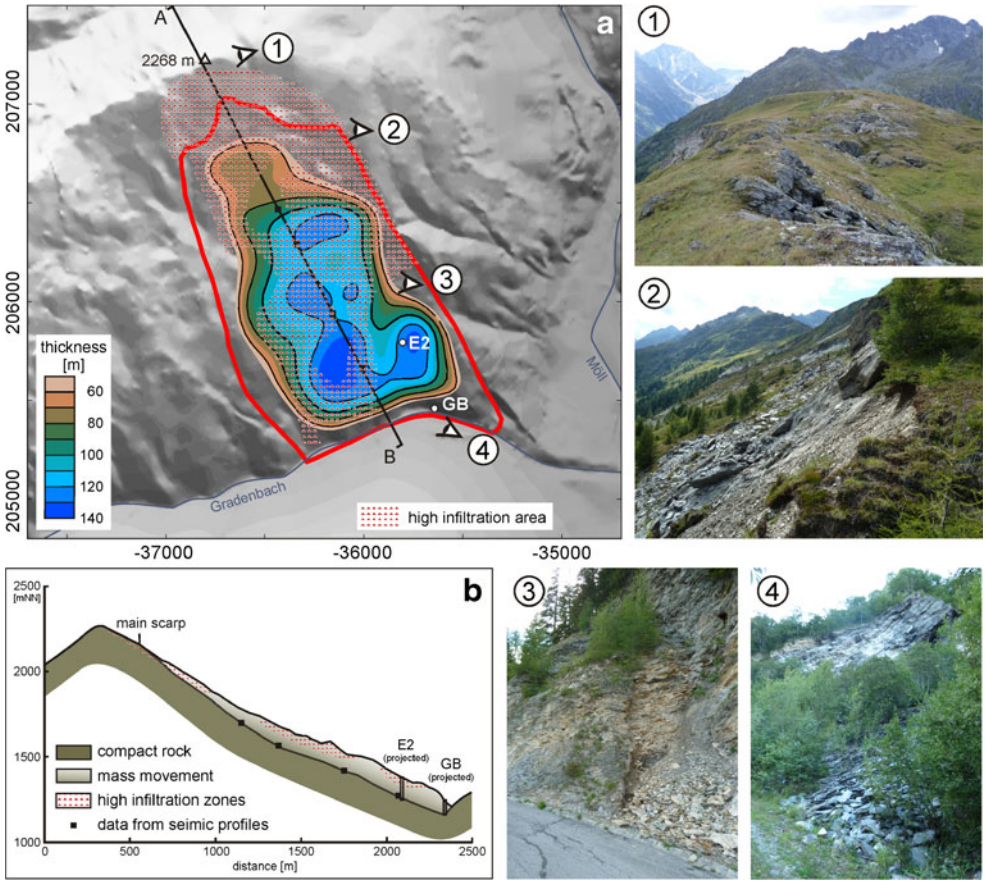

Fig. 3 Morphology and structural model of the GMM. **a** Boundary (*red solid line*) and segmentation of the mass movement (Moser and Glumac 1983) are shown on top of a high resolution DTM (courtesy BEV); *contours* and a *color code* show the thickness of the creeping mass according to Brückl and Brückl (2006); viewpoints of photos *1–4* are marked in the DTM. **b** Cross section through the GMM along the profile *A–B* marked in **a**

(Brückl 1984), a map of the basis of the mass movement (Fig. 3a) was constructed (Brückl and Brückl 2006). A longitudinal cross section through the mass movement is shown in Fig 3b.

A qualitative measure of disintegration and fracturing can be derived from these data. On average, the *P* wave velocities (*Vp*) at the GMM follow the relation (Brückl and Parotidis 2005; Brückl and Brückl 2006):

$$Vp = 455 \times d^{\,0.40}\,\mathrm{m/s} \qquad (1)$$

where *d* is the depth in [m]. Relations similar to Eq. (1) were found in other examples of deep-seated gravitational slope deformation (Brückl and Parotidis 2005). The *P* wave velocities of the rock mass correlate well with the rock porosity (e.g., Watkins et al. 1972; Gardner et al. 1974) and reflect the degree of damage and fracturing of the rock mass. *Vp* of the compact rock below the surface of rupture ranges from 3,800 to 4,500 m/s.

Brückl et al. (2006) used stereoscopic aerial photographs from 1962 and 1996 to construct digital terrain models and orthophotos of the area of the GMM. Images produced by superposition of the orthophotos provided evidence for the delineation of the mass movement. Figure 4a shows the orthophoto derived from the 1996 aerial photograph, showing the boundary of the mass movement which was active between 1962 and 1996. Displacement vectors of materially identical points derived by photogrammetric techniques for the period 1962–1996 (Brückl et al. 2006) are also shown in Fig. 4a. The average horizontal displacement within the mass movement was 19.0±2.2 m. The azimuths of the displacement vectors and the slope gradient are in agreement. The displacement vectors dip more steeply than the slope in the upper part of the mass movement and less steeply in the toe area.

In a first order approximation the mass movement can be described by a simple rotational slider block model with a radius of 5.2 km measured from the center of rotation to the sliding plane (Brückl and Parotidis 2005). Support for this model is obtained by comparing the mass flow through cross sections derived from elevation changes between 1962 and 1996 with the magnitude of the horizontal displacements; the average horizontal velocities through the vertical sections agree well with the average horizontal surface velocities (Brückl et al. 2006).

Figure 4b, c shows enlargements of orthophotos 1962 and 1996 and shows details of the scarp area. The main scarp is clearly outlined in both orthophotos. The increase of the scarp area between 1962 and 1996 corresponds to an average horizontal displacement of ~20 m in the direction of the slope. This figure agrees well with the estimated average horizontal displacement (19.0±2.2 m) and supports the idea of a block movement as an approximation to the actual kinematics of the whole GMM.

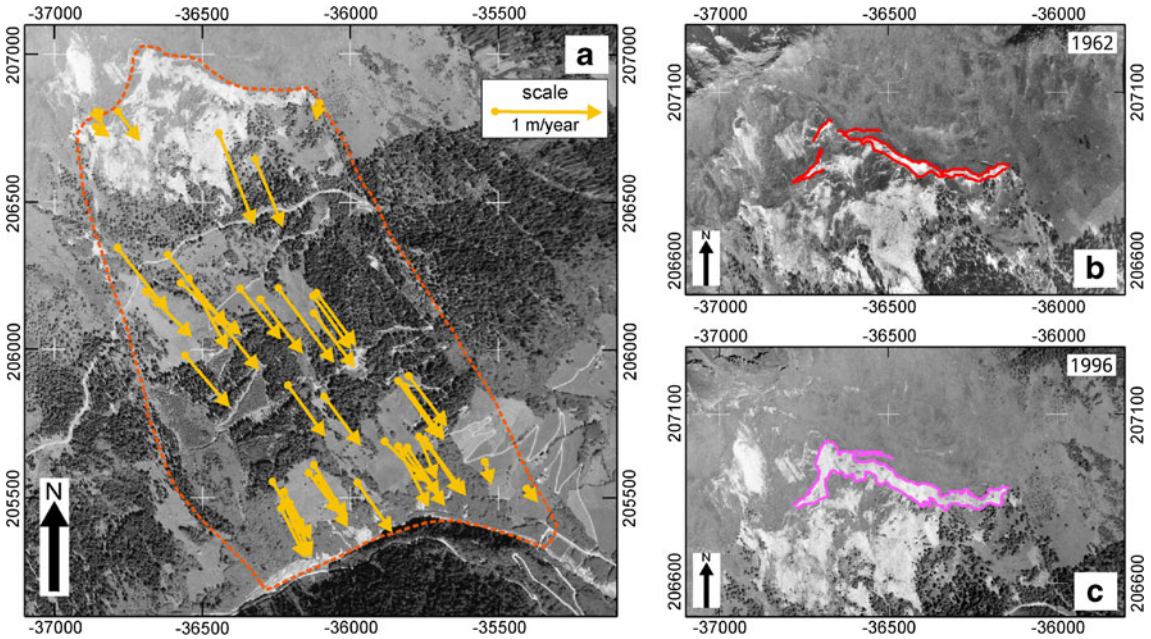

Fig. 4 Photogrammetric evaluation of stereoscopic aerial photographs from 1962 to 1996. **a** Orthophoto 1996; horizontal displacements 1962–1996 are shown by *arrows*. **b** *Red lines* delineate the main scarp area 1962. **c** *Pink lines* delineate the main scarp area 1996

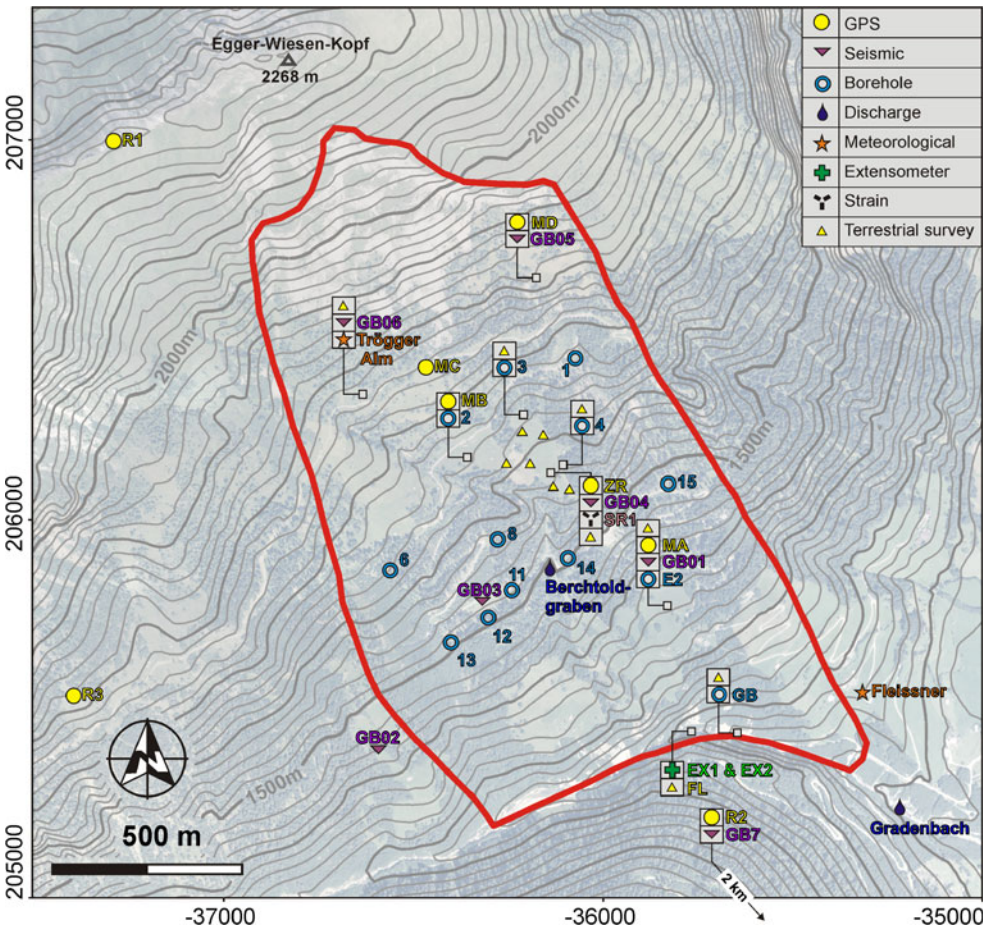

Fig. 5 The Gradenbach Observatory: geodetic, geotechnical (extensometer), meteorological, hydrologic, and seismic monitoring stations

Geodetic and geotechnical measurements and monitoring

Figure 5 provides an overview of the locations of all the relevant measurement and monitoring sites located at the GMM. The geodetic and geotechnical components are described in this section.

GPS

The differential GPS measurements started in July 1999 with two campaigns per year. This schedule has been gradually extended since 2009. Currently, stations R1, R2, MA, and MC are operated continuously throughout the year. They are equipped with GPRS modems, transmitting GPS raw data to the observatory's office at Graz University of Technology, where coordinates are automatically calculated every four hours. The resulting time series are accessible online (http://gbonline.tugraz.at). All the raw data are also copied to data loggers on site. GPS stations MB, MD, and ZR are occupied twice a year with observing sessions of 24 h. Station R3 is occupied occasionally.

Coordinate calculation for stations MB, MD, ZR, and R3 is done interactively. All GPS coordinates refer to base station R2 which is located on stable ground 2 km SE of the landslide. For coordinate calculations (automatic or manual), the software BERNESE 5.0 is used. Since 2009, atmospheric biases are accounted for by using a second reference station (R1): the coordinates and output from BERNESE are scaled to the coordinate difference of baseline R2–R1 (Schön et al. 2005; Schön 2007). The standard deviations of the resulting coordinates are 1 mm in the horizontal direction and 2 mm in the vertical. Slow movements are geodetically traceable even at a considerable distance from the landslide area (stations R1 and R3). The time series of the total displacements are shown in Fig. 6.

Wire extensometer

The steep flanks of the gorge at the foot of the GMM hinder the GPS observations, but enabled us to observe the convergence between the foot of the GMM and the relatively stable rock mass at the opposite valley side (for location see Fig. 5). Two wire extensometers, EX1 and EX2, with wires spanning approximately 50 m across the gorge were installed in 1979 (Kronfellner-Kraus 1980). The analogue readings since 1999 have been manually digitized and outliers edited. In 2006, EX2 was equipped with a continuous electronic recording system.

Since 2002, the extensometer readings were supplemented by terrestrial geodetic measurements. The monitoring point FL (along with two terrestrial monitoring points in its immediate vicinity) is surveyed every year, based on datum points marked in the outcropping rock mass at the relatively stable eastern valley side. The time series of EX2 and FL are shown in Fig. 6 along with the GPS time series. The time series of EX2, FL, and the GPS stations in the lower part of the GMM (MA, ZR) are in good agreement.

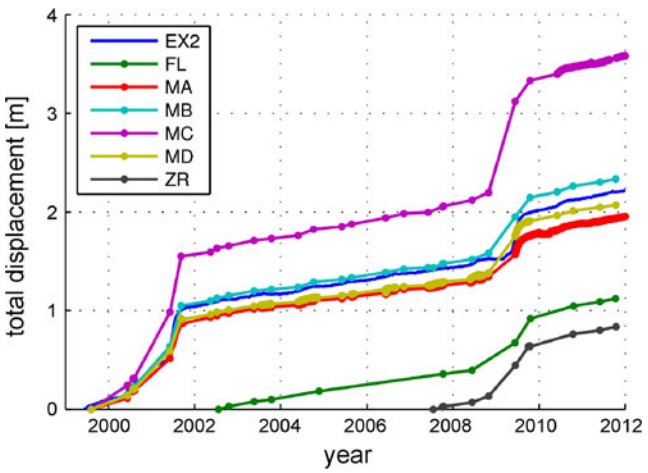

Fig. 6 Time series of the total displacement of GPS stations (MA, MB, MC, MD, ZR), terrestrial surveying point in the gorge (FL), and the wire extensometer EX2 spanning the gorge. For most stations, the *curves* consist of straight lines connecting the results of the surveying campaigns (*points*, usually twice a year). Since 2009 and 2010, the time series of MA and MC, respectively, comprise of daily data points. The extensometer time series is nearly continuous

Strain monitoring by embedded strain rosette and geodetic deformation networks

Temporal changes of strain in the main body of the GMM provide additional information that helps us understand the mechanism of acceleration and deceleration of the landslide. Since 2007, the strain state has been monitored by a strain rosette embedded in the ground.

The strain rosette measures the length variations along three fiber optic sensors in three radial directions and is located in the central part of the GMM (for location see Fig. 5). The rosette sensors are 5 m long and are embedded about 1 m deep in the ground. In 2009, the system was upgraded with an optical multiplexer which facilitates the measurement of the fiber optic sensors sequentially and continuously. The strain rosette is activated from June to October, recording one dataset every day. The variations of the distance between the endpoints of the fiber are measured with an error <2 μm. Processing of the strain rosette data includes correction of the length variations for effects of varying temperature, conversion to strain, and calculation of the 2D strain state (strain ellipse). A precision with a standard deviation of 0.6 microstrains for the half axes of the strain ellipse and 0.1 gon for its orientation is achieved. Brunner et al. (2007) and Wöllner et al. (2011) provide comprehensive descriptions of this measurement system and the evaluation of its data.

Complementary to the installation of the strain rosette, a terrestrial deformation network was established comprising of eight surveying points. The GPS monitoring station ZR is also part of the deformation network. The other deformation network points are at most 150 m away from the strain rosette. Network surveys were carried out in June of 2007, 2008, 2009, and 2011 and in December 2011. Five sets of slant distances, directions, and zenith distances were observed at three network points during each survey. GPS monitoring point MB (100 m outside the network) was incorporated into the network, and point ZR was observed with GPS for a 24-h session. The terrestrial survey data were processed by a free network adjustment using the GPS-derived coordinates of ZR and MB for datum definition. The standard deviations of the resulting coordinates are about 0.5 mm horizontally and 1 mm vertically.

To calculate the strain that occurred between two network surveys, the displacements were separated into a rigid body motion and deformations. The statistically significant trend fitted to the deformations was used to calculate the strain ellipses for any point within the area of the deformation network including the location of the strain rosette. The standard deviations of the half axes of the strain ellipses and their deviations were 28 microstrains and about 7 gon respectively.

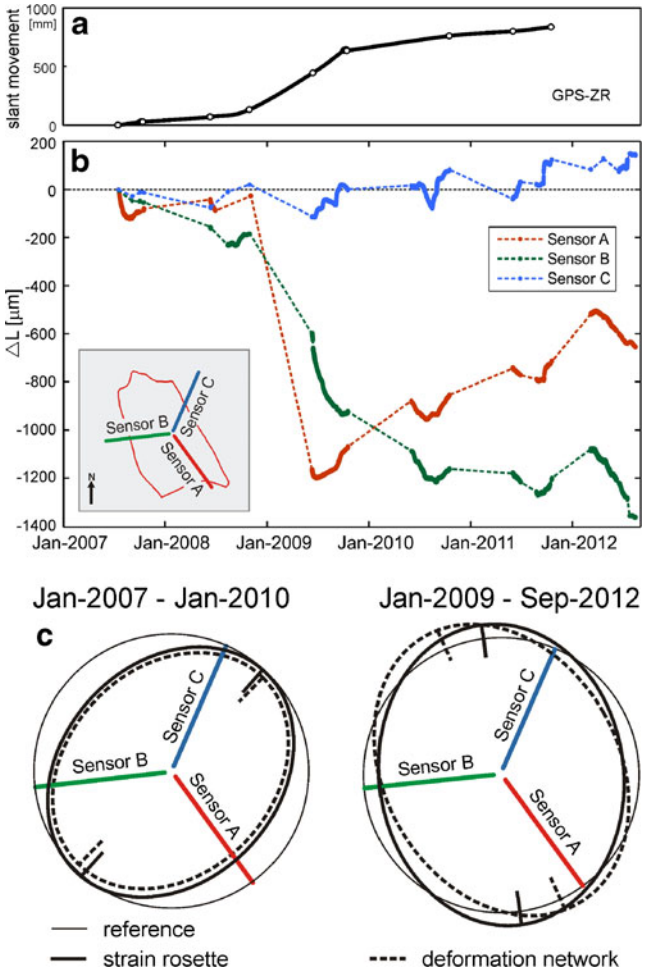

Fig. 7 Monitoring of strain by the strain rosette and a terrestrial deformation network. **a** Total displacement of GPS station ZR (center of strain rosette). **b** Changes in length of the three fibers of the strain rosette (temperature compensated); inset shows orientation of the fiber optical strain sensors. **c** Strain ellipses derived from the strain rosette and the terrestrial deformation network for 2007–2010 and 2009–2012

Figure 7a shows the total displacement of the GPS station ZR from 2007 to 2012. The temperature-corrected readings of the strain rosette are plotted in Fig. 7b. The inset in Fig. 7b shows the orientation of the fiber optic sensors A, B, and C. The orientation of sensor A agrees well the gradient of the slope and the longitudinal direction of the GMM. Figure 7c shows the strain ellipses derived from the strain rosette and the deformation network for the periods 2007–2010 and 2009–2011. A comparison of the strain ellipses, derived from the strain rosette and from the deformation network indicates that both methods of strain determination yield similar results. However, the precision of the strain rosette is significantly higher. During the phase of high sliding velocities in spring 2009, compression in the longitudinal direction of the mass movement took place, whereas thereafter a relaxation of this compression occurred.

Meteorological and hydrological observations

Meteorological and hydrological data are measured continuously and are automated at several locations of the GMM (Lang and Hagen 1999). These measurements are complemented by periodical surveys and field observations (e.g., surveys at snow measuring lines; Lang and Stary 2011).

Precipitation, snow cover, temperature, and other meteorological parameters

Automated meteorological monitoring stations (Fig. 5) are installed at these locations:

Fleissner (precipitation, temperature, air humidity; since 1996)
Trögger Alm (precipitation, airflow and temperature, air humidity, radiation, snow depth; since 2002)
Pichler (precipitation, snow depth; since 1999)

Precipitation in the form of snow has been measured at snow measuring lines since 1997 (Hagen and Lang 2000). These lines were set across forest and open land areas to explore the effect of forests on snow interception. The water equivalent of snow cover is currently measured at 1-week intervals along 14 lines at altitudes between 1,400 and 2,100 m. Each of these lines contains 10 measurement points where snow depth and snow weight is determined to calculate the water equivalent of snow.

Discharge

Discharge is recorded automatically at two stations, on the GMM and at the toe of the GMM (Fig. 5):

Berchtoldgraben (at the open gully; since 1996)
Gradenbach (at the torrent; since 1996)

The discharge measured at Gradenbach captures the entire catchment area of the Gradenbach valley including some small retreating glaciers. The Berchtoldgraben station records mainly the drainage of the central part of the main body of the GMM. The difference in the seasonal distribution of runoff maxima at the Gradenbach and Berchtoldgraben stations is due to the south-east exposure of the GMM and to the fact that the latter is located at a considerably lower altitude than large parts of the catchment area.

Hydrostatic water level

The amount of water penetrating into the main body of the GMM can be observed in boreholes located in the central part of the GMM at altitudes between 1,365 and 1,680 m (Fig. 5). The filter sections have a length of 10 or 12 m and end at depths between 17 and 50 m. Several boreholes have two separate casings with filter sections at different depths which are labeled by lower case letters (e.g., 3a, 3b). Since 2009, automated recording of the hydrostatic water level and water temperature has been carried out at boreholes 3a and 15. The depth to the surface of rupture is mostly >100 m in the area of the borehole gauges and is significantly deeper than the end of the borehole filter casings.

Data 1996–2012

A re-evaluation of the meteorological and hydrological data for the area was carried out for the period 1996–2012. Time series of the precipitation, snow cover water equivalent, discharge at the

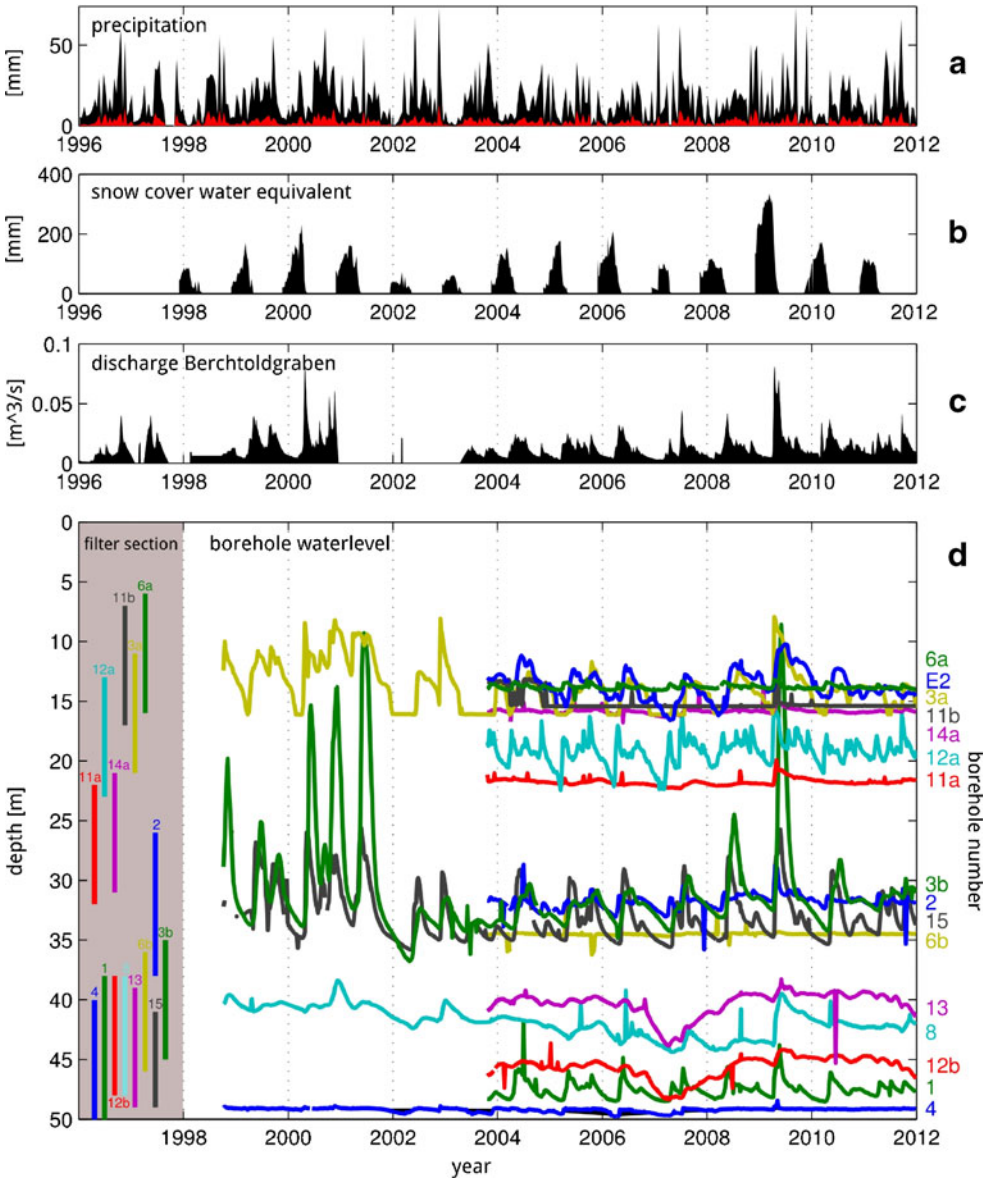

Fig. 8 Meteorological and hydrological time series 1996–2012: **a** precipitation, **b** snow cover water equivalent, **c** discharge of the Berchtoldgraben gauge, and **d** the depth to the hydrostatic water level in the boreholes. The precipitation is computed as the 15-day mean value of daily precipitation (minimum, maximum, and average values). The maximum (*black*) and average (*red*) values are shown. The plotted snow cover water equivalent data are derived from the snow cover measurements of the open land area. The discharge of the Berchtoldgraben gauge is the 15-day average of the daily measured discharge. From 2001 to 2002, the gauge was not operating

Berchtoldgraben gauge, and all the borehole water level recordings are shown in Fig. 8.

The average annual precipitation (rainfall) was about 900 mm. Snowmelt represents a significant contribution to the groundwater regime of the GMM. For the first half of 2009 for example, the potential water input into the hillside of the GMM by snowmelt corresponded approximately to the rainfall during the same period (more than 300 mm). The discharge at the Berchtoldgraben gauge increases immediately at the beginning of the snow melt.

Most of the borehole gauges show a yearly variation with maxima during or just after the snowmelt, i.e., a decrease of snow cover water equivalent in spring. However, the sensitivity of the water level variations in the different boreholes to precipitation and snowmelt varies by more than a factor of 10 and a continuous map of the average hydrostatic water level cannot be constructed. The average height of the hydrostatic level above the end of the filter casing ranges from 0.9 to 15.7 m and averages 7.2 m. There is no significant correlation ($R^2 < 0.02$) between the average height of the hydrostatic level above the end of the filter casing and the depth of the filter casing, indicating that only perched water tables are monitored by the borehole gauges. We conclude that no direct information about the pore water pressure at the rupture surfaces or in the basal sliding zone has been recorded.

Seismic monitoring

Seismic network

The installation of a permanent seismic monitoring network at Gradenbach began in the summer of 2006. The current network comprises of 6 three-component instruments placed on the GMM (Fig. 5). Geospace GS-11D 4.5 Hz 3-component geophones and Reftek 130 recording units are used for data recording, and the stations are solar powered. The nearby reference station GB7 and additional sound sensors help distinguish between seismic events caused by the moving rock mass, very near earthquakes, and surface or atmospheric sources.

Identification of seismic events

The detection of seismic events was done using spectrograms of the seismograms with an applied signal to noise enhancement following the sonogram method described by Joswig (1995). Patterns in the spectrograms representing signals above the noise level were extracted using a seeded region growing algorithm (Gonzales and Woods 2002). The detected patterns were then checked and classified interactively. Earthquakes from global to local scale were identified using earthquake bulletins and nearby observatory stations. Microphone recordings of sonic signals were used to recognize ground movements caused by airborne sound in the seismograms. The remaining events were treated as potential mass movement induced signals (Mertl and Brückl 2007). The further classification of these events was based on the frequency content, the pattern in the spectrogram, and the correlation of the waveform and frequency content among the stations of the network.

During the acceleration phase in the spring of 2009, several types of such potential events were recorded (Fig. 9). Using the classification schemes described above and the correlation of the number of events with the displacement rate of the slope, these events were classified as events induced by the displacement of the slope. Type AA events are short events (duration of 2–4 s) with an impulsive onset. They show high frequency content of up to 100 Hz. Type A events have a similar impulsive onset as type AA events, but they have a longer duration of up to 15 s and a lower frequency content (below 60 Hz). Type B events have weak amplitudes, long duration (10–30 s) and low frequency content with the spectral energy bound to several narrow frequency bands. Type D events are similar to type AA events, but they show an emerging onset and their coda is limited

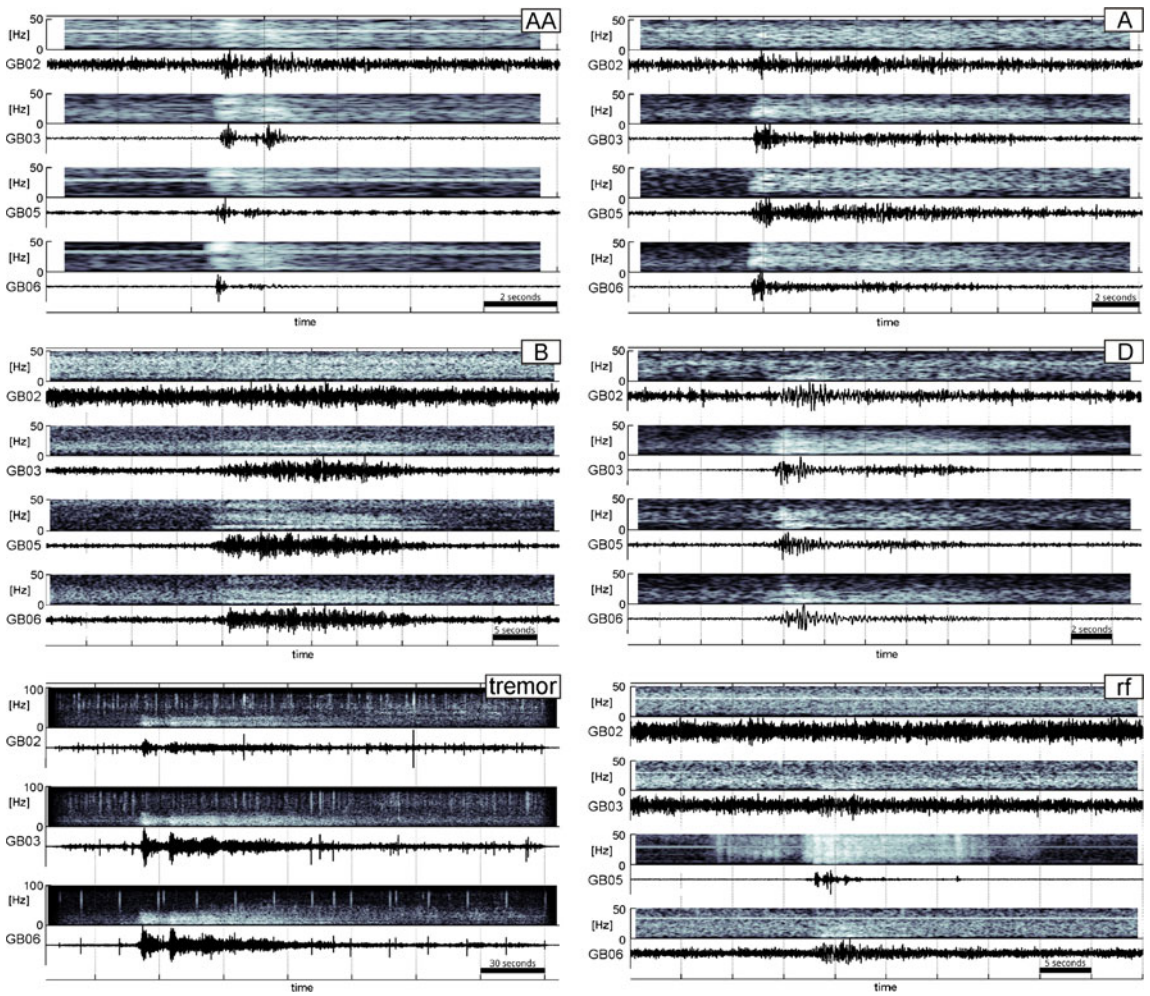

Fig. 9 Seismograms and spectrograms of event types (*AA*, *A*, *B*, *D*, *tremor*, and rock fall (*rf*)) recorded during the episodic phase of high sliding velocity in 2009 at GMM

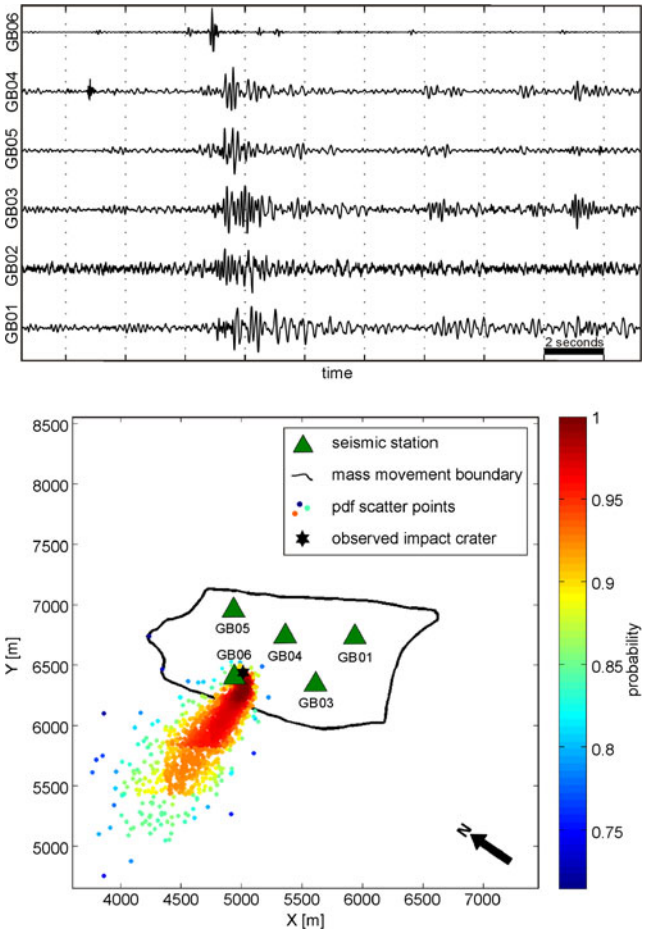

Fig. 10 Location of the impact by a rock fall; **a** seismic recordings at the stations GB01–GB06, **b** location using NonLin Loc, seismic stations are marked by *green triangles*; probability density function (PDF) of trial epicenters are color coded (*color bar*); the most probable epicenter (*asterisk*) corresponds to the highest PDF and density of the trial epicenters

to low frequencies (<20 Hz). The tremor events are long events (>60 s) with the main frequency content below 50 Hz. They show a clear correlation of the waveform and spectral content over the stations on the slope. Type rf events are most likely rockfall events. They show several impulsive high-frequency signals with large amplitudes on one station and a correlating low-frequency and low-amplitude signals on the other stations of the slope.

Location of quakes caused by the mass movement

Location of seismic events is usually based on the arrival times of the seismic phases in the seismograms. The analysis of the events recorded during the phase of high sliding velocities, spring 2009, revealed that most events did not show an impulsive onset, but developed gradually (e.g., type B and type D events in Fig. 9). Moreover, the majority of the recorded events had a very low signal to noise ratio (as low as 1). Therefore, the amount of locatable events, which require a reliable determination of the first onset, is small compared to the total amount of recorded events.

Seismic events which allowed for an accurate picking of the first arrivals were located using the NonLinLoc software (Lomax et al. 2000). For the localization, we created a 3D velocity model based on the seismic *P* wave velocities and structural information derived from active seismic experiments (Brückl and Brückl 2006). NonLinLoc calculates the probability density function (PDF) for the complete model space (e.g., all the possible hypocenters within the searched grid). The PDF provides an intuitive image of the distribution of the possible hypocenters. For sparse seismic networks, this method is to be favored over single point solutions with error-ellipses because it provides a more complete representation of the solution space including multiple local extremes and irregular probability distribution.

An exceptionally powerful rock fall in spring 2009 offered an opportunity to test the accuracy of the applied location method. Figure 10a shows the seismic recordings of this event. The value of the PDF at different hypothetical epicenter locations is shown in Fig. 10b. High values of the PDF and a high density of the hypothetical epicenters mark the most probable solution. The actual impact is marked by an asterisk, which coincides well with the most probable solution. The coordinate system of the seismic velocity model (*x* axis in the direction of the slope of the GMM, *y* axis horizontal) is used in Fig. 10b. During the acceleration phase in spring 2009, seismic events of type A, AA, and D were located. These results are presented in the "Integrated monitoring of the phase of enhanced sliding velocity during spring 2009" section.

Deformation history

The stereoscopic aerial photographs from 1962 represent the earliest high quality documents of the topography of the GMM. An attempt to reconstruct the deformation history as average horizontal displacement back to 1962 is shown in Fig. 11. The following information was used:

- average displacement 1962–1996 determined by photogrammetry (19.0±2.2 m; Brückl et al. 2006)
- average displacement 1969–1991 determined by geodesy at the traverses at 1,800 (9.05±1.8 m) and 1,350 m (7.2±1.3 m; Weidner et al. 1998a)
- steel tape measurements at the foot of the slope 1972–1995 (Weidner et al.1998a)
- wire extensometer measurements at the foot of the slope 1979–2011
- GPS monitoring 1999–2011

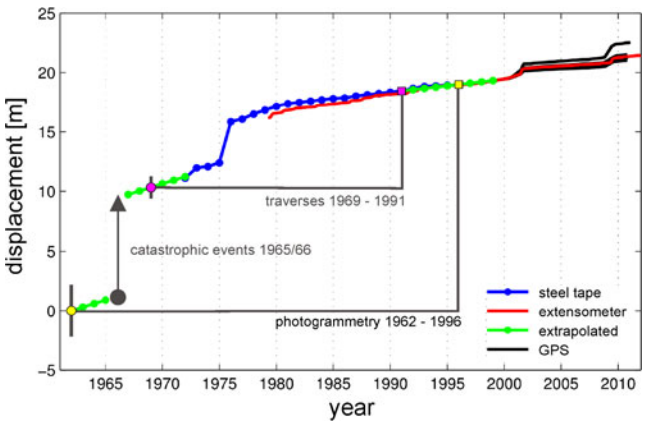

Fig. 11 Reconstruction of deformation history of GMM for the period 1962–2011

The displacement rate of 0.11 m/year derived by Weidner et al. (1998a) for the period 1980–1995 was applied for the period 1991–1999. For 1962–1964 and 1967–1972, we assumed a displacement rate of 0.30 m/year. This value is within the range reported for 1972–1974 by Kronfellner-Kraus (1980) and Weidner et al. (1998a). According to this reconstruction, 8.8 m of horizontal displacement (with the largest error of ±2.2 m resulting from the photogrammetric uncertainty) remain and can be attributed to the catastrophic events 1965 and 1966.

Figure 11 shows clearly the potential of GMM for episodic phases of increased sliding velocities. However, these phases diminish in their intensity after the catastrophic events of 1965 and 1966.

Relation of displacement rate to hydrological parameters

Previous work

The first quantitative investigation of the relation between the hydro-meteorological data and the annual displacement of the Gradenbach slope was carried out by Kronfellner-Kraus (1980). The exponential relation:

$$D = C \times e^{a\,N10} \qquad (2)$$

was fitted to the data. The displacement D during 1 year from 1973 to 1978 was derived from geodetic measurements along profiles between altitudes of 1,300 and 2,000 m. The quantity $N10$ is the total precipitation (including snow melt) of a 10-month period before the main active phase of the slope in spring expressed in [mm]. The free parameters C and a were calculated separately for the periods 1972–1975 and 1976–1978 by Kronfellner-Kraus (1980) to show the efficiency of dewatering of the whole GMM by underground drainage, revetment of gulleys, and afforestation.

Further studies of the influence of hydrology on the movement of GMM were carried out by Moser and Kiefer (1988) and Weidner et al. (1998a, 1998b, 2011). They presented, among other findings, a synoptic representation of cumulative displacement, slope water level at borehole 3a, water equivalents of the snow cover, and precipitation for the period 1979–1994. Between 1980 and 1992, a significant temporal correlation between the high slope water level in borehole 3a and the increased velocity during spring time was observed. The amount of annual displacement also showed a dependency on the deviation of the hydrostatic water level in borehole 3a from the long-term trend.

A proxy of the pore pressure at the surface of rupture

Since the introduction of the concept of effective normal stress into the Coulomb yield criterion, it is understood that pore water pressure significantly influences slope stability (e.g., Bishop 1955; Duncan 1996). Information on the temporal variation of the pore water pressure at the surface of rupture is therefore of fundamental importance. One would expect the best estimate of this physical quantity to be derived from the hydrostatic water level observed in the boreholes. However, as mentioned in the "Meteorological and hydrological observations" section, this data scatter considerably, and most probably only perched water tables within the main body of the GMM are monitored. Because of this lack of direct information on the hydrostatic water level at the surface of rupture or within the basal sliding zone, we derive a proxy of this fundamental quantity from the hydro-meteorological data related to infiltration.

We estimate infiltration from snow melt (free land) and precipitation (Fleissner station). We assume that the weekly reduction of snow cover water equivalent is melt water that contributes 100 % to infiltration. For the corresponding contribution of precipitation we estimated an efficiency of 50 %. The rest is direct run-off. A common and significant feature to the time series of infiltration and the hydrostatic water level is the yearly variation. We constructed the proxy of the hydrostatic water level by fitting the annual variation of the weighted sum of the total monthly infiltration (100 % melt water, 50 % liquid precipitation) to the mean annual variations of the hydrostatic water levels recorded by the borehole gauges. The mean values were calculated by the median in order to reduce the influence of outliers. The selected weights of the actual and 4 previous months were Wp=[0 4 12 8 4]. The correlation between the mean annual variations of the hydrostatic water levels and the proxy is R^2=0.98. The derivation of the proxy from infiltration is illustrated as a filter process in Fig. 12. The time series of the proxy was calculated for the

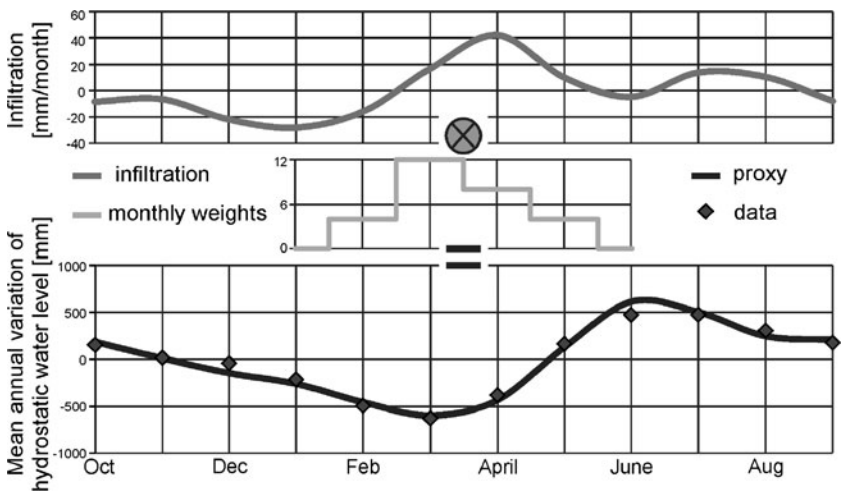

Fig. 12 Modeling of the mean annual hydrostatic water level variations by a proxy computed by convolving the average monthly infiltration (precipitation 50 % and snowmelt 100 %) with the filter operator [0 4 12 8 4]. The coefficients of this operator represent the weights of the infiltration of the current and the 4 preceding months. The average monthly infiltration and the average monthly hydrostatic water level are computed as the median for the period 2003–2012.

whole period of 1996–2012 by filtering the time series of the monthly values of infiltration with the operator *Wp*.

Relations between sliding velocity and hydrological parameters for the period 1996–2012

Subcritical crack growth is a process that may explain the variations of the sliding velocity due to changes of the hydrostatic water level. It allows for progressive damage and brittle deformation of rock masses at stresses well below the material strength. This process commences at stresses which correspond to ~20 % of the critical stress concentration factor or fracture toughness. The velocity of crack growth is proportional to the *n*th power of the applied stress up to ~80 % of the fracture toughness (e.g., Atkinson and Meredith 1989, Fig. 4.1). Dynamic rupture takes place when the stress concentration factor reaches 100 % of the fracture toughness. Values for the exponent n in the range of 20–50 are common for stress corrosion crack growth. However, for diffusion controlled crack growth n is often in the range of 2–10. Atkinson and Meredith (1989) provide a comprehensive review of the phenomenon of subcritical crack growth based on empirical data and the principles of fracture mechanics.

Brückl and Parotidis (2005) introduced the concept of subcritical crack growth as the process which controls the velocity of quasi-continuous deformation of the main body of a mass movement, but also the sliding velocity at the basal surface of rupture. Prager et al. (2008, 2011) also considered subcritical crack growth as a process controlling the development of DGSD. According to Brückl and Parotidis (2005), one fundamental idea is that asperities at the sliding surface must be overcome by subcritical crack growth. The sliding velocity is therefore proportional to the velocity of the subcritical crack growth. The stress concentration factor at the asperities is proportional to the applied stress, which is the Coulomb stress for mode II (sliding) and mode III (tearing) failures. If the effect of the varying crack length on the stress concentration factor is neglected, the sliding velocity v is proportional to the nth power of the Coulomb stress.

We apply as a first approximation a simple one-dimensional slider block model (e.g., Helmstetter et al. 2004) to the GMM to describe the relation between sliding velocity and pore water pressure at the surface of rupture. We consider Terzaghi's principle of effective stress (e.g., Das 1998). Then the Coulomb stress τ_c at the sliding plane is linearly related to the pore pressure or the hydraulic head H at this level.

$$\tau_c = \tau - (\sigma - \gamma_w \times H) \times \tan(\Phi) = \gamma_w \times \tan(\Phi) \times (H + H0) \quad (3)$$

$$H0 = (\tau - \sigma \times \tan(\Phi))/(\gamma_w \times \tan(\Phi)) \quad (4)$$

τ …total shear stress at the sliding surface
σ …total normal stress at the sliding surface
γ_w …unit weight of water
Φ …friction angle of the rock mass at the sliding surface.

The sliding velocity, $V(t)$, is related to the nth power of the temporally varying Coulomb stress τ_c, if subcritical crack growth is the controlling process. We replace the hydraulic head above the sliding surface, $H(t)$, by $proxy(t)$ calculated for the period 1996–2012.

$$V(t) = C1 \times (proxy(t) + H0)^n \quad (5)$$

The unit of $proxy(t)$ and $H0$ is [m] in Eq. 5. According to Brückl and Parotidis (2005), we assume $n=8$ for the exponent in the power law. The constants $C1$ and $H0$ are determined by fitting the integral of the calculated velocities, i.e., the displacement, to the corresponding values observed by the extensometers EX1 and EX2 using a 2D grid search. We chose the comparison with the extensometer data, because the GPS data are not continuous for the whole period 1996–2012. Figure 13 shows the proxy of the mean hydraulic head above the surface of rupture, the displacements calculated by the numerical integration of Eq. 5, and the displacements observed by extensometers EX1 and EX2 for the period 1996–2012. The graph of the calculated displacement was shifted between the corresponding graphs of the displacements observed by EX1 and EX2 by a proper selection of the arbitrary integration constant.

The quasi-stationary phase between 2002 and 2008 and the episodic high velocity phase in spring 2009 are nearly perfectly modeled using $C1 = 5.2 \times 10^{-8}$ m/month and $H0 = 2.55$ m. The beginning of the episodic high velocity phase of 1999–2001 is also quite well simulated. However, there is no indication of the strong acceleration in 2001 in the calculated displacements. Therefore, we need to take into account factors not considered or inaccurately determined by our model. An extension of the precipitation and snow cover time series back to 1962 by correlating with other local meteorological stations could offer the opportunity to model the whole deformation history from 1962 onwards, as reconstructed in Fig. 11. A 2D or even 3D hydraulic and mechanical model would basically allow for a more specific modeling of the infiltration and the buildup of Coulomb stress at the surface of rupture. Future analysis will take advantage of this potential.

Integrated monitoring of the phase of enhanced sliding velocity during spring 2009

Figure 14 shows the result of the localization of seismic events recorded during the phase of enhanced velocity in spring 2009. Accurate travel time picking was possible for 18 events of the A,

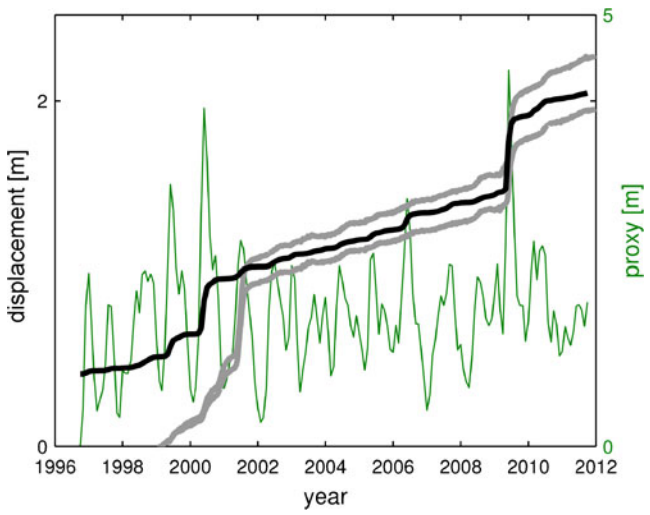

Fig. 13 Prediction of slope movement (*black line*) using the proxy of the hydrostatic water level (*green line*) and Eq. (5). For reference, the data from the extensometer EX1 (*top gray line*) and EX2 (*bottom gray line*) is plotted

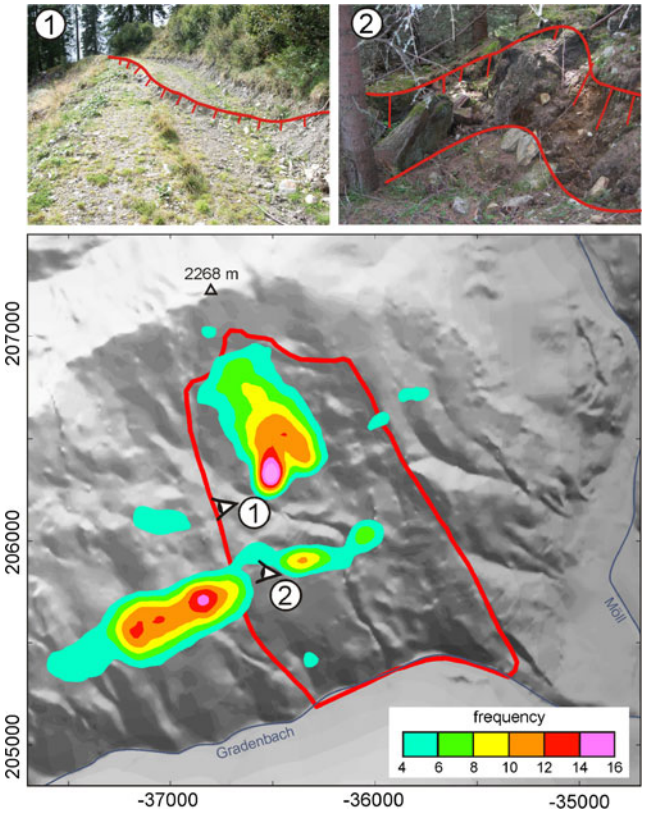

Fig. 14 Spatial distribution of cumulative seismic activity from March to the end of September 2009. The spatial frequency of the possible epicenters with PDF>0.7 is superimposed on the DTM. This quantity represented by a colored contour plot visualizes the area of seismic activity together with the uncertainty of the locations of individual events. Photos from viewpoints *1* and *2* show minor scarps (highlighted by *red signatures*) generated during the phase of high sliding velocities in spring

AA, and D type, and the NonLinLoc method was applied to these data. The colored contours superimposed on the digital terrain model represent the spatial frequency of possible epicenters with a PDF>0.7 on a relative scale for all 18 events. Zones of high seismic activity are (a) the upper part of the GMM and (b) a band orientated almost east–west at lower elevations, with the highest frequencies near the western edge of the GMM. The location accuracy in the second zone (b) is degraded because the epicenters were outside the seismic network. Small scarps (~0.3 m displacement) which developed during the phase of enhanced creep were observed near this zone of high seismic activity (photos 1 and 2 in Fig. 14).

In Fig. 15, the seismic data of the events recorded during the high velocity phase from March 1 to Oct 1 2009 are presented along with geodetic, hydrological, and meteorological data. During this period, 159 events induced by the displacement of the slope were recorded (A, 18; AA, 4; B, 21; D, 59; tremor, 50; rf, 7).

The temporal distribution of the different seismic events shows a significant pattern and a correlation with the geodetic and hydrological time series. At the beginning of April, the seismic activity commenced with type A and D events and most pronounced tremor type events. This phase coincided with the beginning of the snow melt, which is indicated by a sudden decrease of the snow cover water equivalent at the GMM and an increase of discharge at the Berchtoldgraben gauge. The sliding velocity observed by the extensometers (and GPS) did not increase significantly at that time. The tremor events occurred only during a very short period at the beginning of this initial phase with most of the tremor events (43) occurring within 5 days from April 2 to April 6. After April 25, no tremor events were recorded at all.

A second accumulation of seismic activity followed about 2 months later and included all event types apart from tremors. This is the phase of high sliding velocities. Increased discharge at the Gradenbach gauge was also observed at that time. This coincidence may be accidental. The acceleration of the main body of the GMM is accompanied by the occurrence of type B and type rf (rockfall) events which abruptly disappear when the slope begins to re-stabilize at the beginning of June. From this time on, type D events dominate the seismic recordings. Similar to the tremor events, type B events are limited to a narrow time span.

In the period between the first phase of precursor events at the beginning of April and the events correlated with the slope's main displacement, the seismic activity of the GMM ceased completely for about 1 month.

Early warning and hazard estimation

The high accuracy, sensitivity, reliability, and near real-time data availability of the GPS network guarantees the early detection of changes in the creep or sliding behavior of the GMM. Two data sets support the rating of the geodetic indications of an acceleration of the GMM at an early stage.

The hydrostatic water level observed by the borehole gauges responds to precipitation and snowmelt with a time delay of over one month. The proxy we used to estimate the pore pressure at the surface of rupture was created using the weighted sum of precipitation and snow melt data of the 4 months preceding the time of velocity estimation. Thus, we can predict the velocity using Eq. (5) at least one month ahead.

The results from the seismic monitoring motivated us to examine the possibility of implementing the seismic data into early warning and short term prediction. The seismic network was in operation during the period of high velocity in the spring of 2009. An interesting connection was found between the seismic activity and the geodetic and geotechnical (extensometer) measurements of the GMM velocity. Some seismic event types were associated with the periods of high creeping velocities. Other event types were significantly active about 1.5 months before the acceleration of the GMM and can thus be considered as a precursor. This phase coincides exactly with the beginning of the snowmelt. Further analysis and monitoring of the data is needed to clarify if or how the beginning of the snowmelt induces or triggers seismic activity.

Seismic precursors of strong slope deformations were observed around the Steinlehen slide (11.14°E, 47.19°N, Tyrol, Austria) which is smaller but more active than the GMM (Weginger 2012). The seismic precursor of the Steinlehen slide occurred about one week before the acceleration of the slide´s movement. No meteorological or hydrological trigger could be found for this seismic precursor. Therefore, seismic precursors should be taken seriously even if no meteorological indications of acceleration are present. We expect that continuous recording by the strain rosette may also supply precursors if acceleration of the GMM occurs in the future.

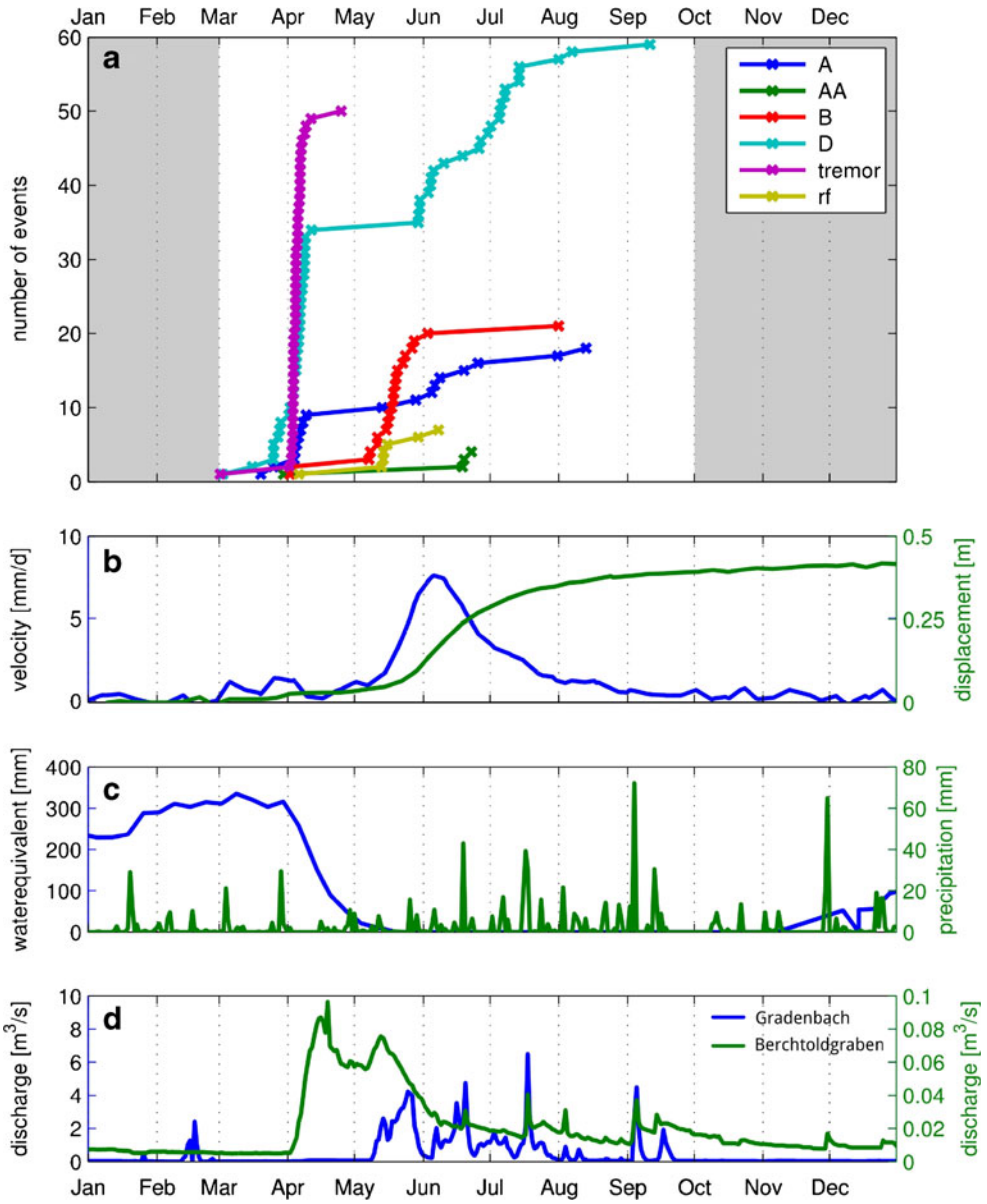

Fig. 15 Seismic activity during the phase of high sliding velocity, spring 2009. **a** The cumulative number of events separated according to their types, **b** the slope's velocity and displacement, **c** the water equivalent of snow cover and precipitation, and **d** the discharge of the Gradenbach (*blue*) and Berchtoldhang (*green*) catchment. Seismic data were systematically analyzed from the beginning of March to the end of September

The close relation between meteorological parameters and sliding velocity implies also the potential to improve our ability to estimate the hazard of a dynamic rupture of the GMM by correlating the hazard potential to estimations of meteorological scenarios. We consider subcritical crack growth as the physical process controlling the velocity and assume a ~8th power relation between the Coulomb stress at the surface of rupture and the velocity (Eq. 5, Fig. 16). We assume that subcritical crack growth begins when the Coulomb stress reaches 20 % of the fracture toughness and the sliding velocity at this stress level is 1 mm/year. With this assumptions and Eq. 5, we are able to relate the proxy and the sliding velocity to the ratio of the Coulomb stress to the fracture toughness.

We see from Fig. 16 that the creep of the GMM would be maintained with a velocity of 1 mm/year, even when the hydrostatic level at the surface of rupture is nearly zero (*proxy* ~0 m). The maximum proxy calculated for the period 1996–2012 was 4.4 m in 2009. This value corresponds to a Coulomb stress of 55 % of the fracture toughness and a velocity of 0.27 m/month. The upper limit of the 8th power law is reached when the proxy reaches 7.5 m, the Coulomb stress is 80 % of the fracture toughness and the velocity rises to 0.18 m/day. The Coulomb stress equals the fracture toughness at a proxy of 10 m. The velocity does not follow the 8th power law when the Coulomb stress exceeds 80 % of the fracture toughness.

In the spring of 2009, the melting of the snow cover with the relative water equivalent of ~0.3 m was mainly responsible for the high proxy and the acceleration of the GMM. A snow cover water equivalent exceeding the 2009 value by a factor 2, together with heavy precipitation during the melting season could cause the

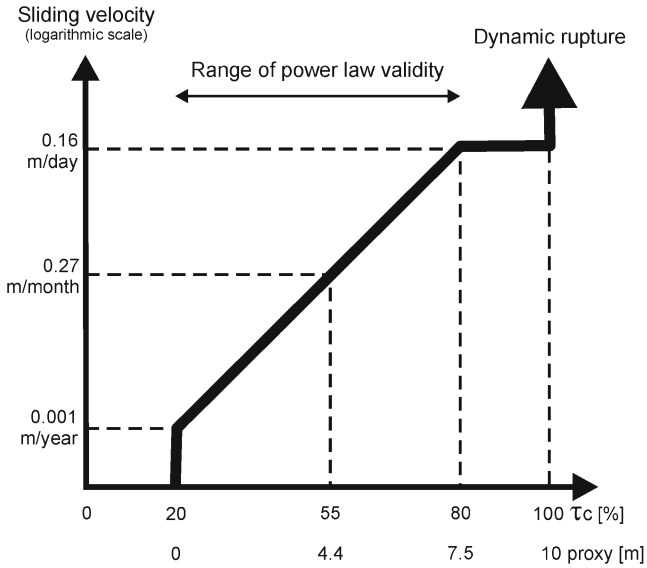

Fig. 16 Schematic diagram showing the sliding velocity as a function of Coulomb stress in the range of subcritical crack growth and the transition to dynamic rupture (modified after Atkinson and Meredith 1989, Fig. 4 (1)). The Coulomb stress is scaled in % of the fracture toughness. Corresponding values of the proxy are also assigned to the *horizontal axis*

Coulomb stress to rise above 80 % of the fracture toughness (*proxy* ~7.5 m) and bring the GMM very close to the state of dynamic rupture. The probability of such weather scenarios should be assessed by meteorologists or climatologists.

Conclusions

The current monitoring and scientific data analysis of the GMM, described in this paper, builds on extensive long-term measurements and a diversity of comprehensive studies, which started after the catastrophic events of 1965/1966. Since 1999, the displacement of the main body of the GMM has been monitored by GPS and extensometers. Precipitation, snow height and water equivalent, temperature, discharge, and hydrostatic water level are monitored by a dense net of partly automated meteorological-hydrological stations. Seismic activity at the GMM is continuously recorded by the local seismic network. Geodetic, meteorological–hydrological, and seismic data relevant for early warning are transmitted to the GBO headquarters in Graz and Vienna and processed by the scientific staff. Real-time as well as periodically retrieved data are archived in data bases and prepared for scientific analysis. With the current capabilities of measurements, data transmission, near real-time processing, and archiving of base data, the geodetic–hydrologic–seismic monitoring of the GMM has achieved a major part of the goals of the GBO.

Snow melt and high precipitation has been identified as the main reason for the phases of high sliding velocity by all the studies that examined this phenomenon at the GMM. A power relation between the velocity of the main body of a mass movement and the Coulomb stress at the surface of rupture should exist if the sliding velocity is controlled by subcritical crack growth. Temporal variations of this Coulomb stress are caused by changes in the hydrostatic water level. Direct evidence of the hydrostatic water level is provided by borehole gauges. However, a brief inspection of the depth ranges of the filter casings and the observed levels reveals that only perched water tables are monitored. A proxy of the hydrostatic water level at the surface of rupture was derived from hydro-meteorological data alone. Using this proxy and the power relation between the velocity and the Coulomb stress, the velocity of the GMM could be modeled to a reasonable degree of accuracy for the period 1999–2012. Estimation of the GMM velocity by this method can be extrapolated more than 1 month ahead and support early warning.

During the last phase of high sliding velocities in 2009, the Coulomb stress reached ~55 % of the fracture toughness. We speculate that extraordinary weather situations (twice the snow cover than that in 2009 and high precipitation during the melting period) could bring the Coulomb stress at the surface of rupture to its critical state and dynamic rupture could not be excluded.

The youngest component within the GBO is the strain rosette. No continuous recording over the whole year is currently feasible. However, intermittent recordings covering the 2009 phase of high sliding velocities revealed initial longitudinal compression with a succeeding extensional relaxation as significant mechanical processes.

Continuous seismic monitoring has been carried out in the GBO since 2006. During the most recent phase of high sliding velocities in 2009, significant changes in seismic activity preceded and accompanied the geodetically observable acceleration. Based on these and similar observations at another, smaller landslide in the Eastern Alps we believe that seismic monitoring can support short term prediction and early warning of a dangerous acceleration of the GMM. The many different types of seismic events accompanying the phase of high sliding velocity contain valuable information on the deformation mechanism. However, the extraction of this information will be a task for future work.

Acknowledgments

The authors gratefully acknowledge funding for this research by the Austrian Academy of Sciences within the frame of ISDR. The authors express their thanks also to Dr. J. Brückl for the compilation of geological data and maps. Thanks also to three anonymous reviewers and the journal editor for their constructive suggestions for improving the quality of the paper.

References

Atkinson BK, Meredith PG (1989) The theory of subcritical crack growth with applications to minerals and rocks. In: Atkinson BK (ed) Fracture Mechanics of Rocks. Academic Press Geology Series, London, pp 111–166

Bishop AW (1955) The use of the slip circle in the stability analysis of slopes. Geotechnique 5(1):7–17

Brückl E (1984) Bericht über seismische Untersuchungen im Bereich des Talzuschubes im Gradenbach. Mitteilungen der Forstlichen Bundesversuchsanstalt, Wien 153:69–73

Brückl E, Brückl J (2006) Geophysical models of the Lesachriegel and Gradenbach deep-seated mass movements (Schober range, Austria). Eng Geol 83:254–272

Brückl E, Parotidis M (2005) Prediction of slope instabilities due to deep-seated gravitational creep. NHESS 2005(5):155–172

Brückl E, Brunner FK, Kraus K (2006) Kinematics of a deep-seated landslide derived from photogrammetric, GPS and geophysical data. Eng Geol 88:149–159

Brunner FK, Zobl F, Gassner G (2003) On the Capability of GPS for Landslide Monitoring. Felsbau 21(2):51–54

Brunner FK, Woschitz H, Macheiner K (2007) Monitoring of deep-seated mass movements. 3rd Int. Conf. Structural Health Monitoring of Intelligent Infrastructure. CD-Proceedings, Vancouver, p 9
Das BM (1998) Principles of Geotechnical Engineering, 4th edn. PWS PUBLISHING COMPANY, Boston, 712 pp
Dramis F, Sorriso-Valvo M (1994) Deep-seated gravitational slope deformations, related landslides and tectonics. Eng Geol 38:231–243
Duncan JM (1996) Soil slope stability analysis. In: Turner AK, Schuster RL (eds.) Landslides: investigation and mitigation, Washington, pp 337–371
Fügenschuh B, Seward D, Mancktelow N (1997) Exhumation in a convergent orogen: The western Tauern Window. Terra Nova 9:213–217
Gardner GHF, Gardner LW, Gregory AR (1974) Formation velocity and density - the diagnostic basics for stratigraphic traps. Geophysics 39:770–780
Gonzalez RC, Woods RE (2002) Digital image processing - second edition, Prentice Hall
Hagen K, Lang E (2000) Schneehydrologische Untersuchungen im Einzugsgebiet des Gradenbaches (Kärnten). FBVA-Berichte, Wien, 116:68 pp
Häusler H (1974) Gutachten über das geologische System des Talzuschubes im kritischen Gefahrenbereich des Gradenbaches als Grundlage bautechnischer Sicherungsmaßnahmen, 25.1.1974, 146 pp. for reference see Weidner (2000)
Helmstetter A, Sornette D, Grasso J, Andersen JV, Gluzman S, Pisarenko V (2004) Slider block friction model for landslides; application to Vaiont and La Clapiere landslides. JGR 109: B02409
Joswig M (1995) Automated classification of local earthquake data in the BUG small array. GJI 120:262–268
Kronfellner-Kraus G (1974) Die Wildbacherosion im allgemeinen und der Talzuschub im besonderen. Wien, Sonderdruck aus „100 Jahre Forstliche Bundesversuchsanstalt", pp 309–342
Kronfellner-Kraus G (1980) Neue Untersuchungsergebnisse in Wildbächen - Der Talzuschub in Abhängigkeit von Niederschlägen. Int. Symp. Interpraevent. Bad Ischl 1:179–192
Lang E, Hagen K (1999) Wildbacheinzugsgebiet Gradenbach: Analyse des Niederschlag- und Abflussgeschehens 1968–1996. FBVA-Berichte, Wien 108:109 pp
Lang E, Stary U (2011) Multifunctional Monitoring in Torrent Catchments. Die Bodenkultur, Journal for Land Management, Food and Environment, Universität für Bodenkultur Wien 62:71–76
Lomax A, Virieux J, Voant P, Berge C (2000) Probabilistic earthquake location in 3D and layered models: Introduction of a Metropolis-Gibbs method and comparison with linear locations. In: Thurber, CH, Rabinowitz N (eds.), Kluwer Academic Publishers: pp101-134
Mertl S, Brückl E (2007) Observation of fracture processes in creeping rock masses by seismic monitoring. Proceedings of 11th Congress of the ISRM, Lisbon, Portugal 9–13 July 2007
Moser M, Glumac S (1983) Geotechnische Untersuchungen zum Massenkriechen in Fels am Beispiel des Talzuschubes Gradenbach (Kärtnen). Verhandlungen der Geologischen Bundesanstalt, Wien 3:209–241
Moser M, Kiefer J (1988) Die hydrologischen Verhältnisse und ihre Beziehungen zur Kinematik im Bereich der Talzuschubsmasse Gradenbach / Kärnten. Steirische Beiträge zur Hydrogeologie 39:95–115
Prager C, Zangerl C, Patzelt G, Brandner R (2008) Age distribution of fossil landslides in the Tyrol (Austria) and its surrounding areas. NHESS 8:377–407
Prager C, Ostermann MA, Zangerl C (2011) Time-dependent rock slope weakening processes: evidence from dated landslides in the Eastern Alps. Geophys Res Abstr 13:EGU2011–13787
Schmid SM, Fügenschuh B, Kissling E, Schuster R (2004) Tectonic map and overall architecture of the Alpine orogen. Eclogae Geol Helv 97:93–117
Schön S (2007) Affine Distortion of small GPS networks with large height differences. GPS Solutions 11:107–117
Schön S, Wieser A, Macheiner K (2005) Accurate Tropospheric Correction for Local GPS Monitoring Networks With Large Height Differences, ION GNSS 18th Int. Technical Meeting of the Satellite Division, Long Beach, CA:250–260
Watkins JS, Walters LA, Godson RH (1972) Dependence of in-situ compressional wave velocity on porosity in unsaturated rocks. Geophysics 37:29–35
Weginger S (2012) Detektion und Lokalisierung von seismischen Ereignissen zur Überwachung der Aktivität der Massenbewegung Steinlehnen. Diploma Thesis, Vienna University of Technology: 92 pp
Weidner S, Moser M, Lang E (1998a) Influence of hydrology on sagging of mountain slopes ("Talzuschübe") - New results of time series analysis. 8th International IAEG Congress, Vancouver, Canada, Balkema, pp 1259–1266
Weidner S, Moser M, Lang E (1998b) Zeitreihenuntersuchungen an Talzuschüben. Freiburger Forschungshefte: Bergbau und Geotechnik, Freiburg A847:63–77
Weidner S, Moser M, Lang E (2011) Geotechnische und kinematische Analyse des Talzuschubes Gradenbach (Kärnten/Österreich). Jahrbuch der Geologischen Bundesanstalt, Wien 151(1–2):17–60
Wöllner J, Woschitz H, Brunner FK (2011) Testing a large optical strain-rosette, embedded in a landslide area. 8th International Symposium on Field Measurements in Geomechanics 2011, September 2011. Proceedings, Berlin, pp 12–15

E. Brückl (✉) · S. Mertl
Department of Geodesy and Geoinformation,
Vienna University of Technology,
Gusshausstrasse 27/29, 1040, Vienna, Austria
e-mail: ebrueckl@mail.tuwien.ac.at

F. K. Brunner · M. Müller
Institute of Engineering Geodesy and Measurement Systems,
Graz University of Technology,
Steyrergasse 30, 8010, Graz, Austria

E. Lang · U. Stary
Department of Natural Hazards and Alpine Timberline,
Federal Research and Training Centre for Forests, Natural Hazards and Landscape (BFW),
Hauptstrasse 7, 1140, Vienna, Austria